The Astronomical Journal, 162:61 (16pp), 2021 August https://doi.org/10.3847/1538-3881/ac0057

Stellar Activity Manifesting at a One-year Alias Explains Barnard b as a False Positive

Jack Lubin[1], Paul Robertson[1], Gudmundur Stefansson[2,18], Joe Ninan[3,4], Suvrath Mahadevan[3,4], Michael Endl[5], Eric Ford[3,4,6], Jason T. Wright[3,4], Corey Beard[1], Chad Bender[7], William D. Cochran[8], Scott A. Diddams[9,10], Connor Fredrick[10,11], Samuel Halverson[12], Shubham Kanodia[3,4], Andrew J. Metcalf[9,10,13], Lawrence Ramsey[3,4], Arpita Roy[14,15], Christian Schwab[16], and Ryan Terrien[17]

[1] Department of Physics and Astronomy, University of California, Irvine, 4129 Frederick Reines Hall, Irvine, CA 92697, USA
[2] Department of Astrophysical Sciences, Princeton University, 4 Ivy Lane, Princeton, NJ 08540, USA
[3] Department of Astronomy and Astrophysics, The Pennsylvania State University, 525 Davey Laboratory, University Park, PA 16802, USA
[4] Center for Exoplanets and Habitable Worlds, The Pennsylvania State University, 525 Davey Laboratory, University Park, PA 16802, USA
[5] McDonald Observatory and Center for Planetary Systems Habitability, The University of Texas at Austin, Austin, TX 78730, USA
[6] Institute for Computational & Data Sciences, The Pennsylvania State University, University Park, PA 16802, USA
[7] Steward Observatory, University of Arizona, 933 N Cherry Avenue, Tucson, AZ 85721, USA
[8] McDonald Observatory and Center for Planetary Systems Habitability, The University of Texas at Austin, Austin TX 78712, USA
[9] Time and Frequency Division, National Institute of Standards and Technology, 325 Broadway, Boulder, CO 80305, USA
[10] Department of Physics, University of Colorado, 2000 Colorado Avenue, Boulder, CO 80309, USA
[11] Associate of the National Institute of Standards and Technology, Boulder, CO 80305, USA
[12] Jet Propulsion Laboratory, California Institute of Technology, 4800 Oak Grove Drive, Pasadena, CA 91109, USA
[13] Space Vehicles Directorate, Air Force Research Laboratory, 3550 Aberdeen Ave SE, Kirtland AFB, NM 87117, USA
[14] Space Telescope Science Institute, 3700 San Martin Drive, Baltimore, MD 21218, USA
[15] Department of Physics and Astronomy, Johns Hopkins University, 3400 N Charles Street, Baltimore, MD 21218, USA
[16] Department of Physics and Astronomy, Macquarie University, Balaclava Road, North Ryde, NSW 2109, Australia
[17] Department of Physics and Astronomy, Carleton College, One North College Street, Northfield, MN 55057, USA
Received 2021 March 24; revised 2021 April 30; accepted 2021 May 5; published 2021 July 15

Abstract

Barnard's star is among the most studied stars given its proximity to the Sun. It is often considered the radial velocity (RV) standard for fully convective stars due to its RV stability and equatorial decl. Recently, an $M \sin i = 3.3 M_{\oplus}$ super-Earth planet candidate with a 233 day orbital period was announced by Ribas et al. New observations from the near-infrared Habitable-zone Planet Finder (HPF) Doppler spectrometer do not show this planetary signal. We ran a suite of experiments on both the original data and a combined original + HPF data set. These experiments include model comparisons, periodogram analyses, and sampling sensitivity, all of which show the signal at the proposed period of 233 days is transitory in nature. The power in the signal is largely contained within 211 RVs that were taken within a 1000 day span of observing. Our preferred model of the system is one that features stellar activity without a planet. We propose that the candidate planetary signal is an alias of the 145 day rotation period. This result highlights the challenge of analyzing long-term, quasi-periodic activity signals over multiyear and multi-instrument observing campaigns.

Unified Astronomy Thesaurus concepts: Exoplanet astronomy (486); Stellar activity (1580)

Supporting material: machine-readable table

1. Introduction

In the 105 yr since its discovery by E.E. Barnard as the star with the largest proper motion (Barnard 1916), Barnard's star (GJ 699) has become one of the most studied and heavily scrutinized star systems. Adding to its distinguishing characteristics, it is the nearest star to our own Sun in the northern celestial hemisphere, and the second-closest star system overall (Bailer-Jones et al. 2018; Gaia Collaboration 2021). This proximity has engendered fascination by astronomers in many subfields of astronomy.

All of these qualities have made the star attractive to astronomers in exoplanet science for decades. In 1963, Peter van de Kamp believed he had detected an astrometric wobble of Barnard's star using Swarthmore College's 24 inch refractor at Sproul Observatory (van de Kamp 1963), which he attributed to a planet. He later updated his findings three more times, proposing a second planet in the system (van de Kamp 1969), and then revising the orbital parameters of both planets twice, finally concluding the system comprised 0.7 $M_{\rm J}$ and 0.5 $M_{\rm J}$ planets orbiting with periods of 12 and 20 yr, respectively (van de Kamp 1975, 1982).

The 1975 and 1982 revisions were published in spite of two earlier results challenging the validity of those planets' detections. In the first, Hershey (1973) used van de Kamp's photographic plates to determine that all the stars in the field of Barnard's star appeared to wobble in concert, and the source of this variability could be traced to telescope and instrumentation upgrades at times concurrent with the shifts in the data. Additionally, Gatewood & Eichhorn (1973) reported no astrometric wobble of Barnard's star using the Van Vleek and Allegheny Observatories at Wesleyan University and University of Pittsburgh, respectively. More recent studies have confirmed that van de Kamp's planets are not recoverable by instruments that ought to have detected them easily (Benedict et al. 1999; Kürster et al. 2003; Choi et al. 2013; Ribas et al. 2018, hereafter R18).

The Doppler, or radial velocity (RV), method for planet detection has its own challenges for low-amplitude signals. Currently, the most prominent source of false positives is stellar activity. This activity, which results from phenomena such as starspots and plages, is modulated by the stellar rotation; it can

[18] Henry Norris Russell Fellow.

induce RV signals that mask or masquerade as planets (Robertson et al. 2014, 2015). As our instruments become more precise, we are finding that even the quietest stars are indeed variable below $1\,\mathrm{m\,s^{-1}}$. Furthermore, the interaction between stellar activity signals and other signals, such as planets, can worsen aliasing, which can occur when reconstructing a signal from incomplete sampling (Robertson et al. 2014). The quasi-periodic nature of these stellar-activity-induced signals, coupled with the inherently uneven sampling in astronomical observations, creates conditions for signal aliasing. Stellar activity is difficult to model and predict, but it has been shown that observing in the near-infrared (NIR) can help mitigate the effect of starspot-dominated activity (Marchwinski et al. 2015); however, the amount of mitigation is limited based on the target star's effective temperature and the impact of magnetic fields on line profile changes (Reiners et al. 2010). Despite the problems that stellar-activity-induced signals create, these signals often decay away with time. Therefore, we are more confident in the planetary origin of a signal when it persists for much longer than the typical spot lifetime, although we have seen spot signals on M dwarfs persist for longer than we might expect for Sun-like stars (Robertson et al. 2020).

When surveying old M-dwarf stars like Barnard's star, the problem of stellar-activity-induced signals is exacerbated due to the lifetimes of spots. Starspots on G-type stars will typically survive ~3 stellar rotations (depending on spot size; Giles et al. 2017), but a starspot on the surface of an old M-dwarf star might live through many more rotations of the star. (Robertson et al. 2015, 2020; Davenport et al. 2020). Furthermore, while the average G-type star has a stellar rotation period of 10–20 days (Nielsen et al. 2013; McQuillan et al. 2014), Old M dwarfs can have rotation periods in excess of 100 days (Newton et al. 2016a; Suárez Mascareño et al. 2018). Therefore, we can expect starspot and active region RV signals on old M-dwarf stars to maintain high signal power for hundreds to thousands of days. This creates a unique problem: such a timescale is long enough for signals to be measured across multiple consecutive observing seasons. When the stellar rotation period begins to rival a significant fraction of the observing season, the conditions for significant aliasing are firmly in place. Further complicating the matter for M dwarfs, the periods at which stellar-activity-induced signals exist—namely, the rotation period, its harmonics, and aliases—can coincide with the periods we would expect for a planet orbiting in or near the star's habitable zone (Kopparapu et al. 2013; Newton et al. 2016b; Vanderburg et al. 2016).

Barnard's star is often referred to as a Doppler standard star for its relatively quiet nature, RV stability, high apparent brightness, and equatorial decl. Through this combination of factors, it is widely considered as the RV standard for fully convective stars (e.g., Bean et al. 2010; Anglada-Escudé & Butler 2012). Such standard stars are vital to the exoplanet community for instrument commissioning and calibration. As our instruments become more precise, we may find planets and/or activity signals for all stars. It is crucial that we fully understand and characterize the signals associated with whichever stars we designate as standards so that we can continue to have standard stars at all.

The Habitable-zone Planet Finder (HPF) began observing Barnard's star in the spring of 2018 for engineering purposes. At the time, the star was not known to host a planet. Shortly after, R18 announced a super-Earth planet candidate orbiting Barnard's star with a 232.8 ± 0.4 day orbital period. Metcalf et al. (2019) presented early observations of the star to demonstrate the near-infrared RV precision achievable with HPF and its laser comb but did not discuss the planet candidate due to the relatively short observational span compared to the period of the signal. As we continued to observe the star, we still did not find clear evidence of a signal at 233 days. This, combined with the findings from Kürster et al. (2003), which found a correlation between the RVs and Hα values for Barnard's star, prompted us to revisit the full RV data set and the corresponding activity tracer time series.

After our own analysis of the original discovery data set and the addition of new data from HPF, we find that the signal at 233 days is transitory in nature and is an alias of the 145 ± 15 day rotation period as reported by Toledo-Padrón et al. (2019): $\left(\frac{1}{145} - \frac{1}{365}\right)^{-1} = 240$. The 233 day proposed period is well within the 1σ uncertainty on the rotation period. We are therefore compelled to conclude that the RV data of Barnard's star is best explained without the planet Barnard b proposed by R18.

This paper is organized as follows. In Section 2, we outline the data sources, split into the discovery data set (Section 2.1) and the subsequent modifications we made to create an updated data set (Section 2.2). In Section 3, we perform the experiments of model comparison (Section 3.1), periodogram analysis (Section 3.2), and sampling sensitivity (Section 3.3). In Section 4, we discuss the ramifications of this false-positive result and in Section 5 we conclude.

2. Data

2.1. Discovery Data

The claim by R18 of a 233 day planet candidate orbiting Barnard's star was based on a data set that was assembled over a 20 yr span using multiple Doppler spectrometers. These instruments included those which employed the iodine-cell (I_2) method (Valenti et al. 1995; Butler et al. 1996): 186 points from the High Resolution Échelle Spectrometer (HIRES; Vogt et al. 1994) installed on the 10 m Keck I Telescope at Maunakea in Hawaii; 43 points from the Automated Planet Finder (APF; Vogt et al. 2014) installed on the 2.4 m telescope located at Lick Observatory on Mt. Hamilton outside of San Jose, California; 75 points from the UVES spectrograph installed on the 8.2 m VLT UT2 at Paranal Observatory in Chile (Dekker et al. 2000); and 39 points from the Planet Finder Spectrometer (PFS; Crane et al. 2010) installed on the 6.5 m Magellan II located at Las Campanas Observatory in La Silla, Chile. Other instruments used for data collection include 187 points and 40 points from the HARPS (Mayor et al. 2003) and HARPS-N (Cosentino et al. 2012) spectrometers, respectively, installed on the ESO 3.6 m at La Silla in Chile and the 3.5 m Telescopio Nazionale Galileo at La Palma, and lastly 201 points from the visible channel of the CARMENES spectrograph (Quirrenbach et al. 2016) installed on the 3.5 m telescope at Calar Alto Observatory in Spain.

In all, 771 RV points were used. Further detailed information on the data sources and reduction methods can be found in R18. For ease of reference herein, we have dubbed this the discovery data set.

In addition to RV data, R18 provided the time series of Ca II H&K (S_{HK}) and Hα indices for the instruments where either or both of these activity tracers are available. S_{HK} and the Hα

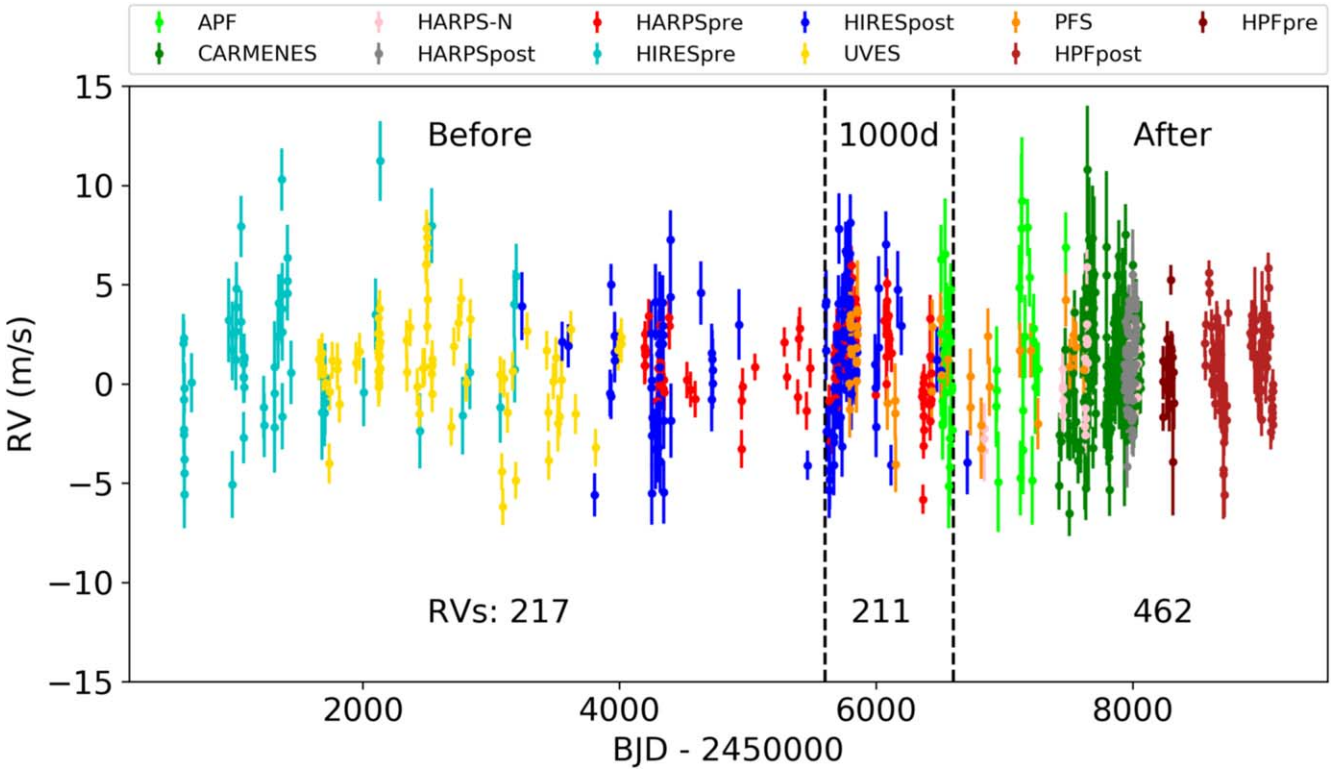

Figure 1. The entire updated RV time series spanning 23 yr. Our three time windows of interest are noted along with their number of observations. Excluding HPF, the After window has 343 observations. Instrumental zero-point offsets have been applied.

index are known tracers of stellar activity, which measure the filling in of the photospheric lines from heating in the chromosphere due to increased magnetic flux.

2.2. Updates to Data

We made a few updates to the discovery data set. The first concerned the UVES Hα time series. R18 published 21 Hα points alongside 75 RV points, originally from Zechmeister et al. (2009). We noticed a nonuniform offset in time between Hα epochs and seemingly corresponding RV epochs of $\sim$0.5 days. Therefore, we manually changed the Hα time stamps to equal the nearest corresponding RV time stamp for consistency.

Next, we substituted more recent reductions of the RV data for certain instruments for the (now) older reductions used by R18. First, we used the velocities from the reduction of HIRES data provided by Tal-Or et al. (2019a). Additionally, we split the HIRES data into "pre" and "post" with respect to the instrument's CCD upgrade in 2004 August. This was motivated by Tal-Or et al. (2019a), who fit an offset, but we kept this as a free parameter when modeling for completeness. As several nights in this reduction contain multiple observations, we performed a nightly binning by taking a weighted average with weights σ_{RV}^{-2}. This binning preserved the sampling used by R18, except the updated time series includes one additional epoch at BJD = 2453301.74204. We excluded the last observation at 2456908.73079 because the associated velocity of 53.319 m s^{-1} makes it a $\sim$5.5σ outlier. We confirmed that this data set had been corrected for secular acceleration.

We similarly used the velocities from the reduction of HARPS data as performed by Trifonov et al. (2020). We used the RVs that had been corrected for secular acceleration, nightly zero-point offsets, and drift. Again, we maintained "pre" and "post" designations with respect to the HARPS fiber upgrade in 2015 for completeness (Lo Curto et al. 2015). These data included more observations than were originally included in R18, with 108 observations occurring within an 11 day period in 2013 May. These observations were taken as a part of the Cool Tiny Beats (CTB) program (Berdinas et al. 2017). Comparison between the CTB observations and the original HARPS data suggested that R18 performed a nightly averaging to compile their data set, but they do not describe exactly how they performed this binning. We chose to use a nightly weighted average with the same weights as described above.

The last modification to the discovery data set was the addition of the HPF data (Section 2.3). For ease of reference herein, we have dubbed the new data set as the updated data set. This updated data set includes the original, unaltered APF, CARMENES, HARPS-N, and PFS data; the UVES data with time stamps adjusted; the new data reductions of HIRES and HARPS (both split into pre and post domains); and the new HPF data; see Figure 1.

2.3. HPF Data

HPF is a high-resolution ($R \sim 55{,}000$) NIR spectrograph on the 10 m Hobby–Eberly Telescope (HET), covering the Doppler-information-rich z, Y, and J bands from 810 to 1280 nm (Mahadevan et al. 2012, 2014). To enable precise RVs in the NIR, HPF is temperature stabilized to the sub-millikelvin level (Stefansson et al. 2016). HET is a fully queue-scheduled telescope (Shetrone et al. 2007), and all observations were obtained as part of the HET queue. HPF has an NIR laser-frequency comb (LFC) calibrator, which has been shown to enable $\sim$20 cm s^{-1} calibration precision in 10 minute bins and 1.53 m s^{-1} RV precision on-sky on Barnard's star (Metcalf et al. 2019) over an 3

month baseline. In this paper, we extend this baseline to 856 days. Stefansson et al. (2020) further discusses our drift correction algorithms. To enable maximum RV precision with HPF, we obtained all of our Barnard's star observations using the HPF LFC simultaneously with the on-sky observations.

To test the on-sky RV measurement performance of HPF, we observed Barnard's star as part of the HPF Commissioning and ongoing Engineering time due to its brightness, overall known Doppler RV stability, and its rich RV information content in the NIR. Due to the restricted altitude design of the HET, the HET can only observe Barnard's star at certain times of the nights, or "tracks," for approximately 68 minutes at a time. In total, we obtained 1016 high-quality spectra in 118 HET tracks with a median signal-to-noise ratio (S/N) of 479 per extracted 1D pixel evaluated at 1 μm. Due to a planned instrument thermal cycle in 2018 August, which led to a minor RV offset before and after the cycling, we place an explicit RV offset before and after this event in our RV modeling. Before the thermal cycle, we generally obtained six exposures of Barnard's star with an exposure time of 300 s in each HET track, while we generally obtained 10 exposures with an exposure time of 183 s in each HET track after the thermal cycle. This change was made in order to harmonize the observing strategy of Barnard's star with that employed for the rest of the HPF 5 yr blind Doppler survey. This standardized the observing for different targets according to their brightness, minimizing any potential risk of saturation for bright targets such as Barnard's star. The observing setup for Barnard's star has remained the same since the thermal break installation.

Overall, the 1016 high-quality spectra had a median exposure time of 191 s and a median photon-limited RV precision of 2.36 m s^{-1}. After performing a weighted average of RV points within a given HET track, we obtain a median RV precision of 0.77 m s^{-1} per binned RV point. We use the binned RV points for subsequent analysis, which can be found in Table 1 in Appendix B.

The 1D HPF spectra were reduced from the H2RG up-the-ramp data using the algorithms and procedures described in Ninan et al. (2018), Kaplan et al. (2018), and Metcalf et al. (2019). Following the 1D spectral reduction, we calculated precise RVs of Barnard's star using an adapted version of `SERVAL` (SpEctrum Radial Velocity AnaLyzer; Zechmeister et al. 2018), optimized to analyze HPF spectra as further discussed in Metcalf et al. (2019) and Stefansson et al. (2020). To derive precise RVs, `SERVAL` uses the template-matching algorithm, which has been shown to be particularly effective at producing precise RVs for M dwarfs (Anglada-Escudé & Butler 2012). To estimate accurate flux-weighted barycentric velocities, we used the `barycorrpy` package (Kanodia & Wright 2018), which uses the methodology and barycentric-correction algorithms presented in Wright & Eastman (2014). Following Metcalf et al. (2019) and Stefansson et al. (2020), to derive the RVs we only use the eight HPF orders cleanest of tellurics, covering the wavelength regions from 8540–8890 Å and 9940–10760 Å. To minimize the impact of telluric and sky-emission lines on the RV determination, we explicitly mask out such lines as described in Metcalf et al. (2019) and Stefansson et al. (2020). We subtracted the estimate sky background from the target spectra using the dedicated HPF sky fiber.

3. Analysis

We have taken a three-pronged approach to our investigation of the 233 day signal, largely performing the same experiments on both the discovery and updated data sets. First, we model the system's activity and/or potential planet with Gaussian process (GP) regression models to identify a preferred model. Next, we perform a periodogram analysis to show the transitory nature of the signal. Finally, we analyze subsets of the data to show how the signal power is concentrated in time.

3.1. Model Comparison

We began our analysis by modeling the stellar activity and/or planet signals for both the discovery and updated data sets. We chose to model stellar activity signals with GP regression because the GP framework has proven especially adept at modeling quasi-periodic signals associated with stellar rotation (Haywood et al. 2014; Rajpaul et al. 2015; Suárez Mascareño et al. 2020; Bortle et al. 2021).

In order to better constrain the stellar rotation signal, we first modeled the activity tracers using GP regression. We used a modified version of `Radvel` (Fulton et al. 2018), which uses logarithmic priors for the GP hyperparameters, setting broad priors as advised by Angus et al. (2018). We used the `Celerite` package (Foreman-Mackey et al. 2017) for its efficiency. Specifically, we use the celerite-compatible replacement for the quasi-periodic kernel for the covariance between the ith and jth observations:

$$k_{ij} = \frac{B}{2+C}\exp\left(\frac{-|t_i - t_j|}{L}\right)\left[\cos\left(\frac{2\pi|t_i - t_j|}{P_{\rm rot}}\right) + (1+C)\right] + \sigma^2\delta_{ij},$$

equivalent to Equation (56) in Foreman-Mackey et al. (2017). The hyperparameters of this kernel have similar interpretations to the quasi-periodic kernel function: B is related to the signal amplitude, L is the decay timescale for the exponential term in days, C is a scaling term, σ^2 is the jitter from additional white noise beyond what can be accounted for in the formal measured uncertainties, and $P_{\rm rot}$ is the recurrence timescale of the signal in days; in this case our astrophysical interpretation is closely related to the stellar rotation period. Each instrument received its own B and σ hyperparameters, but all instruments shared global C, L, and $P_{\rm rot}$ hyperparameters.

We first performed a GP regression model to the discovery data set's Hα values. Table 4 shows our priors and subsequent maximal posteriors from this fit. The resulting posterior value for $\log C = -5.85$ indicates that the signal in question, i.e., the stellar rotation, is highly periodic in nature. Toledo-Padrón et al. (2019) state a rotation period of 145 ± 15 days, and from the results of our GP model of the Hα data, we are able to achieve a consistent result at $143.7^{+11.83}_{-10.93}$ days. Performing a GP with the same priors on hyperparameters for the S_{HK} time series yielded similar results.

Using the Hα posteriors of the $\log L$, $\log C$, and $P_{\rm rot}$ terms as the priors in the RV model, we ran a suite of models on the RVs from the discovery data. In all of these RV models, the $\log C$ posterior value continued to prefer negligibly small values. We quickly found a similar behavior with the $\log B$ hyperparameter for APF as we had for the $\log C$ parameter. We

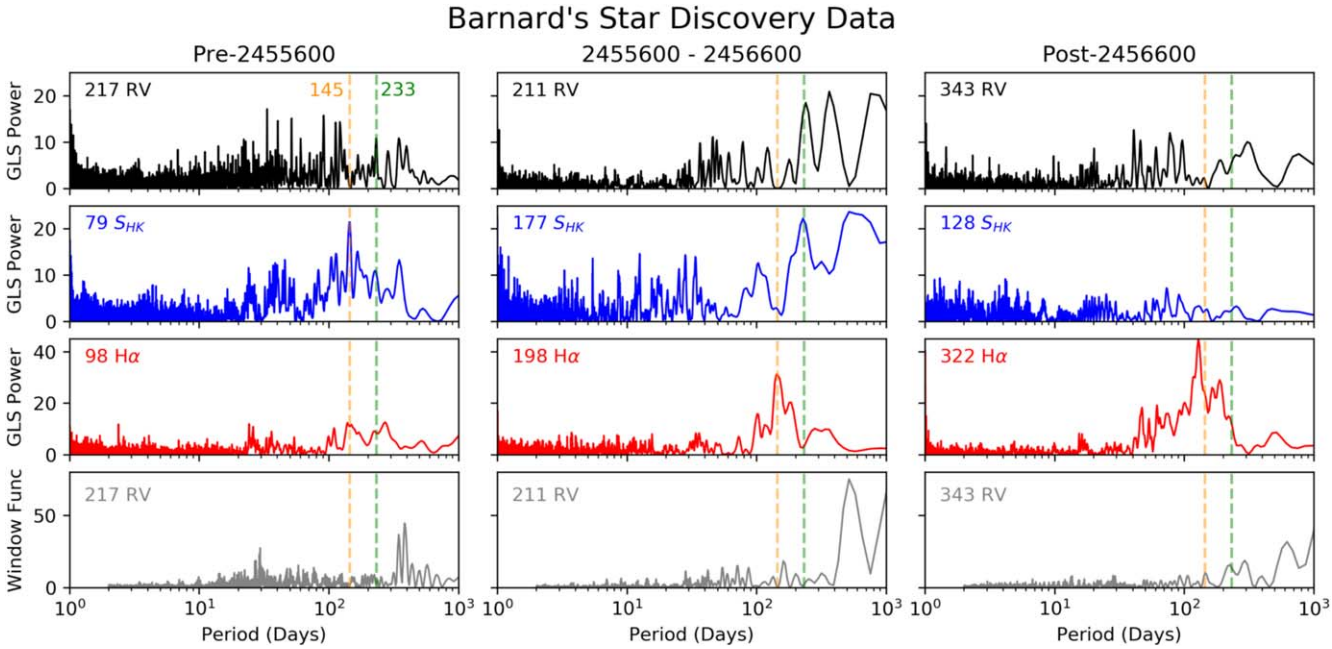

Figure 2. GLS periodograms of the discovery data time series broken down into three time windows. The middle column is the 1000 day window. The 233 day signal is only present at significant power in the 1000 day window in both the RVs (black) and Ca H&K S values (blue). The Hα index (red) traces the rotation period. The window function for the RV time series in each window is the last row in gray. The orange line indicates 145 days, the stellar rotation period, and the green line indicates 233 days, the proposed planet period.

believe that, due to the small aperture and iodine calibration on such a faint and red target star, the variability in the APF data is due primarily to photon noise rather than correlated astrophysical variability. We therefore opted to perform all analyses without a GP term for the APF RVs. When modeling activity, APF was allowed only an instrumental jitter and offset term, while when considering a planet, APF data were modeled with a Keplerian and instrumental jitter and offset only.

We computed three models on the discovery data set's RVs: a GP fit only, a 233 day planet fit only, and a GP + 233 day planet fit. Table 2 in Appendix C shows the resulting Bayesian information criteria (BIC) and the number of free parameters in each model. We compare models by their ΔBIC, preferring more complex models to simpler models when $\mathrm{BIC}_{\mathrm{simple}} - \mathrm{BIC}_{\mathrm{complex}} > 10$ (Kass & Raftery 1995). For the discovery data, this criterion is satisfied for the GP-only model compared to the Planet-only model, but it is not satisfied for the GP+Planet compared to the GP-only one. Thus, the GP-only model is our preferred model. We then repeated this experiment of model comparisons using the updated data set. We used the same priors as for the discovery data set, and we achieved a similar result, as shown in Table 3. The GP+233 day model has the smallest BIC, but the ΔBIC between this model and the GP-only model does not justify the more complex model's additional free parameters, and so therefore the GP-only model is once again our preferred model. The posteriors for all models using the discovery data can be found in Tables 4 and 5, and using the updated data in Table 6 in Appendix C.

3.2. Periodograms

After finding the preferred model to be one that accounts for stellar activity only, we set out to determine how the activity signal might have revealed itself as a planetary signal in the GLS periodogram of the RV time series.

In an attempt to show the coherence of the planetary signal, we split the discovery data into roughly equal thirds by observation number (taking care to not cut in the middle of an observing season) and computed the generalized Lomb–Scargle periodogram (GLS; Zechmeister & Kürster 2009) of each block of data. The 233 day signal is strongly present in the middle third, as shown in Figure 2. Given some idealized data set, which has comparable quality data, sampling, and white noise in all subsets of time, a true planetary signal must persist in all subsets. It will stay in phase across the entire observational time baseline, and the loss of power from removing a fixed number of data should be consistent regardless of which specific data are removed. While this data set is not such a perfect data set, the result of this test was the first indication that the 233 day signal is not planetary in nature.

We then divided the corresponding S_{HK} values in the same manner and, after computing GLS periodograms for each block, we saw similar behavior. Notably, in the time window when the RV signal at 233 days is strongest, there is a matching peak in the S_{HK} periodogram. This result is similar to Hatzes (2013), where it was shown that activity signals changing over seasonal time spans can imprint planet-like periodicity into the RV time series.

From these early results, we performed a season-by-season, instrument-by-instrument analysis of the discovery data in an effort to identify tighter, more scientifically grounded boundaries for splitting the data. We found that for both the Hα and the S_{HK} time series, the rotation period of the star, 145 ± 15 days (Toledo-Padrón et al. 2019), is recoverable in the 2011 season by visual inspection when plotting out the data. Through this, we realized that the 233 day signal persisted with a significant power only for a 1000 day stretch of time—from BJD 2,455,600 to 2,456,600, 211 observations (see Figure 1)—during the observing seasons of 2011, 2012, and 2013). For ease of communication, we have subsequently

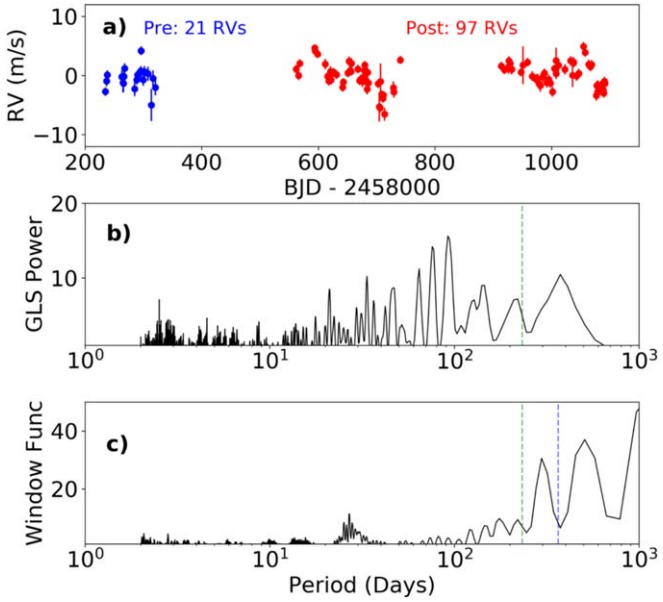

Figure 3. Top: the HPF RV time series split into "pre" (blue) and "post" (red) with respect to the thermal break. Middle: the GLS periodogram for the HPF RVs. The green dashed line is at the proposed planet period. Bottom: the accompanying window function periodogram. The blue dashed line denotes 365 days.

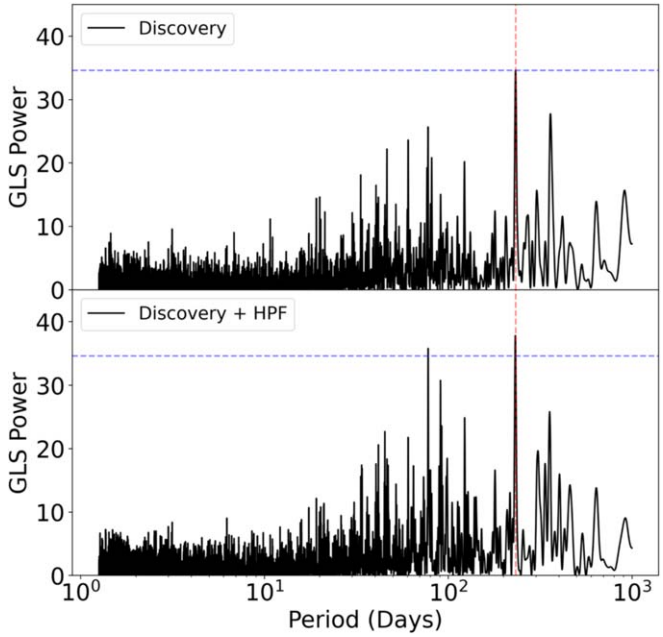

Figure 4. A comparison of the GLS periodograms for two different data sets. The addition of HPF data to the original discovery data set only marginally increases the strength of the peak at 233 days, while the peak at 77 days, the first harmonic of the rotation period, greatly increases. The horizontal blue dashed lines are set at the height of the peak at 233 days in the discovery data set and are intended to guide the eye.

designated this time span as the 1000 day window. From here on, we begin referring to time with respect to the 1000 day window: the before, during, and after epochs. The RV and activity periodograms in Figure 2 show the behavior of the 233 and 145 day signals in each of our three epochs.

When we stitch back together the before and after RVs of the discovery data set to create a data set with 560 points, albeit with a noticeable gap in the center, we still do not see any significant power at the 233 day period. In fact, the GLS power of the 233 day signal drops from ∼31 down to ∼15. As GLS power scales exponentially with significance, this loss in power corresponds to a large loss in statistical significance. Additionally, the 233 day signal loses its place as the top peak in favor of a 45 day signal.

With this in mind, we turned to the new HPF data. Figure 3 shows the time-series HPF RVs as well as its periodogram and window function. We do not see evidence for a signal at 233 days. This could be due to a combination of the fact that HPF is an NIR spectrograph, which is less susceptible to spot-dominated stellar activity than a visible spectrograph, and/or the star could have been less active in the last few years than it was in 2011–2013. The top peak in the HPF data's GLS periodogram is at 92 days. We believe this peak is part of a comb of aliases of the ∼75 day (second peak) first harmonic of the rotation period.

With the addition of 118 new data points, we would have expected the power of the signal at the proposed planet's period to increase. Adding the HPF RVs to the discovery data set (note this is not the same as our updated data set because it still includes the original reductions of the HARPS and nonsplit HIRES data sets), we recover the signal at 233 days in a GLS periodogram at nearly the same power as is found when only considering the discovery data alone ($\Delta\text{Power} \simeq 3$) while the signal at 77 days has a large increase in power ($\Delta\text{Power} \simeq 10$); see Figure 4. As explored in detail in Section 3.3.2, the HPF RVs do not increase the power at 233 days as much as would be expected for a genuine exoplanet. When we exclude the 1000 day window observations from this combined data set, the 233 day signal again loses significant power and no longer retains its place as the top peak in the periodogram.

Lastly, we have chosen to demonstrate the transitory nature of the 233 day signal with the Lomb–Scargle periodogram due to the broader community's common understanding of the algorithm. Regardless of the periodogram we used (Bayes Factor, Marginalized Likelihood (Feng et al. 2017); Compressed Sensing (Hara et al. 2017)), when we remove the observations in the 1000 day window we see the same result. The strength of the 233 day signal is almost entirely contained within the 211 data points that compose the 1000 day window.

3.3. Sampling Sensitivity

Such a dramatic reduction in signal significance by the exclusion of certain data prompted us to ask if it was reasonable to remove 27.6% of the data (the percentage of the RV time series that is inside the 1000 day window for the discovery data set) and still expect a signal to persist. In an effort to address this, we created subsets of data where we removed RV points from the time series and computed the GLS periodogram of the resulting subset.

3.3.1. Random Removal

First, we experimented with an approach of randomly removing data. We created 2000 different subsets of the discovery data where 211 observations—the same number as are found in the 1000 day window—were randomly removed. For the first 1000 subsets, we allowed the randomizer to choose any observations for removal (except for the first and last observations, as we did not want to change the baseline of the time series in any subset). In the second 1000 subsets, we

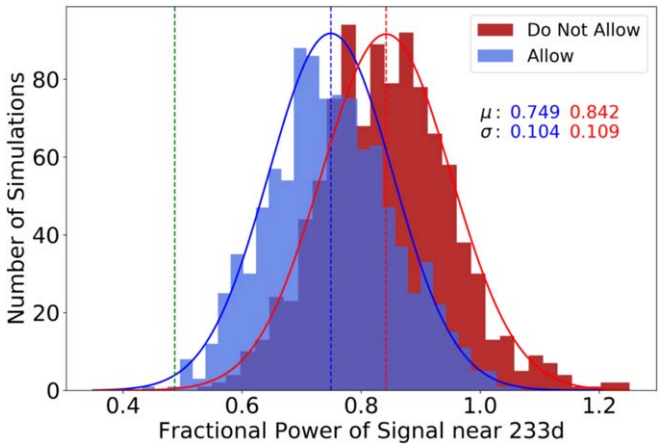

Figure 5. Histograms of the GLS Power from randomly removing 211 observations from the discovery data set in 1000 subsets via two different methods: where we allow for observations within the 1000 day window to be part of the random removal (blue) and for when we do not allow those observations to be part of the random removal (red). The green line indicates the subset that corresponds to removing only the 211 observations that make up the 1000 day window. Gaussian best-fit parameters are shown in their respective colors.

enforced that the randomizer not choose any observations that were taken during the 1000 day window (as well as the first and last observations again). This is an important distinction because it tests how localized the signal is by keeping the data where we believe all of the signal power lies.

For each subset, after removing the randomly selected observations, we recalculated and removed zero-point instrumental offsets and then computed the GLS periodogram. In each subset's periodogram, we tracked how the power of the signal at 233 days was affected by the removal of data. Figure 5 shows the fractional power (normalized by the true power of the signal when all discovery data are included) of a signal peak nearest to 233 days within a ± 3 day span (in fact, we see the same results when expanding this as far as ± 20 days) in each of these two rounds of subsets.

For those where we allowed for any observation to be removed, the average loss in power of the 233 day peak is 25%. By fitting a Gaussian distribution to the ensemble of subsets, we see that when we remove the specific 211 observations that make up the 1000 day window, the resulting subset constitutes a 2.5σ outlier. For those subsets where we do not allow for removal of any observations from the 1000 day window, the average loss of power is less, only 16%. This result is consistent with our hypothesis that the power of the 233 day signal lies mostly in the 1000 day window. A Gaussian fit to this ensemble shows the removal of the specific 1000 day window observations is a 3.25σ outlier. Furthermore, and equally important, for both methods of removal there are subsets of the discovery data where the significance of the 233 day signal actually increases, by up to 20%. These increases are notable because they indicate there are subsets where the removal of data significantly strengthens the proposed planet signal.

3.3.2. Consecutive Removal

Next, we performed a similar analysis wherein we removed 211 consecutive data points, by a process we call rolling omission. First, we fit for instrumental zero-point offsets. We created an algorithm to start with an observation, remove the subsequent 211 points, compute the GLS periodogram for the subsequent subset of the data, and track the fractional power of the signal (data subset power at 233 days/full data set power at 233 days). Then, increment to the next starting observation and repeat for the next subsequent 211 observations. Because we did not want to create a subset with a different baseline than the full data set, the first iteration began with the removal of the second observation and the last iteration began with the observation equal to $N - 211 - 1$, where N is the total number of observations in the time series. We performed this test on both the discovery and updated data sets, but the results are more illuminating with the addition of the HPF data in the updated data set, primarily because with more data points, the algorithm is able to run longer before reaching the end.

To show the results' deviation from expectation more clearly, we performed the rolling omission test on synthetic data in which we include a planet signature. We created synthetic data sets where for each time stamp and associated error of the real observations, we calculated the corresponding expected velocity for a planet with the same parameters as published in R18. Then we added a white noise term to each velocity. Noise was drawn from a Gaussian centered at zero with width equal to the error measurement for the observation at that time stamp. We created 10 of these synthetic data sets and ran the rolling omission test on each one, averaging the results.

Figure 6 shows the result of the rolling omission test on the updated data set (black points) and the averaged synthetic data sets (gray points) as a function of both observation number and time. The vertical green line indicates the iteration of rolling omission where the subset removed matches exactly the removal of the specific 211 observations of the 1000 day window. The green shading shows the width of the 1000 day window in index and time-stamp space. The red vertical line shows the iteration of rolling omission where the first point of the consecutive removal is equal to the first observation in the CARMENES time series. Like in the random removal experiments, this experiment shows that the loss in fractional power when we remove the specific 211 observations that make up the 1000 day window is far greater than the average (black dashed line).

In addition, the tests on synthetic data sets track a nearly horizontal line, showing that for a signal that persists throughout the span of the data, the loss in power from removing consecutive chunks of data is nearly agnostic to the window that is removed. When the data are dense in time, as they are toward the end of the data set, the fractional power begins to decrease. However, for the real data set, we see just the opposite behavior: the fractional power increases dramatically after the red vertical line, even going above 1.0. This means that as we remove some of the best data, in terms of nightly cadence, RV precision, and redder instruments less susceptible to spot-dominated stellar activity in the case of the HPF and CARMENES data, the signal becomes stronger and more significant than if we include all of the data. This is because we are removing data that do not actually contain a signal at 233 days, thus concentrating the subset on the observations that truly contain the signal.

Through these tests we became convinced that not only does nearly all of the signal power of the proposed planet lie in the particular 211 RVs that make up the 1000 day window, but

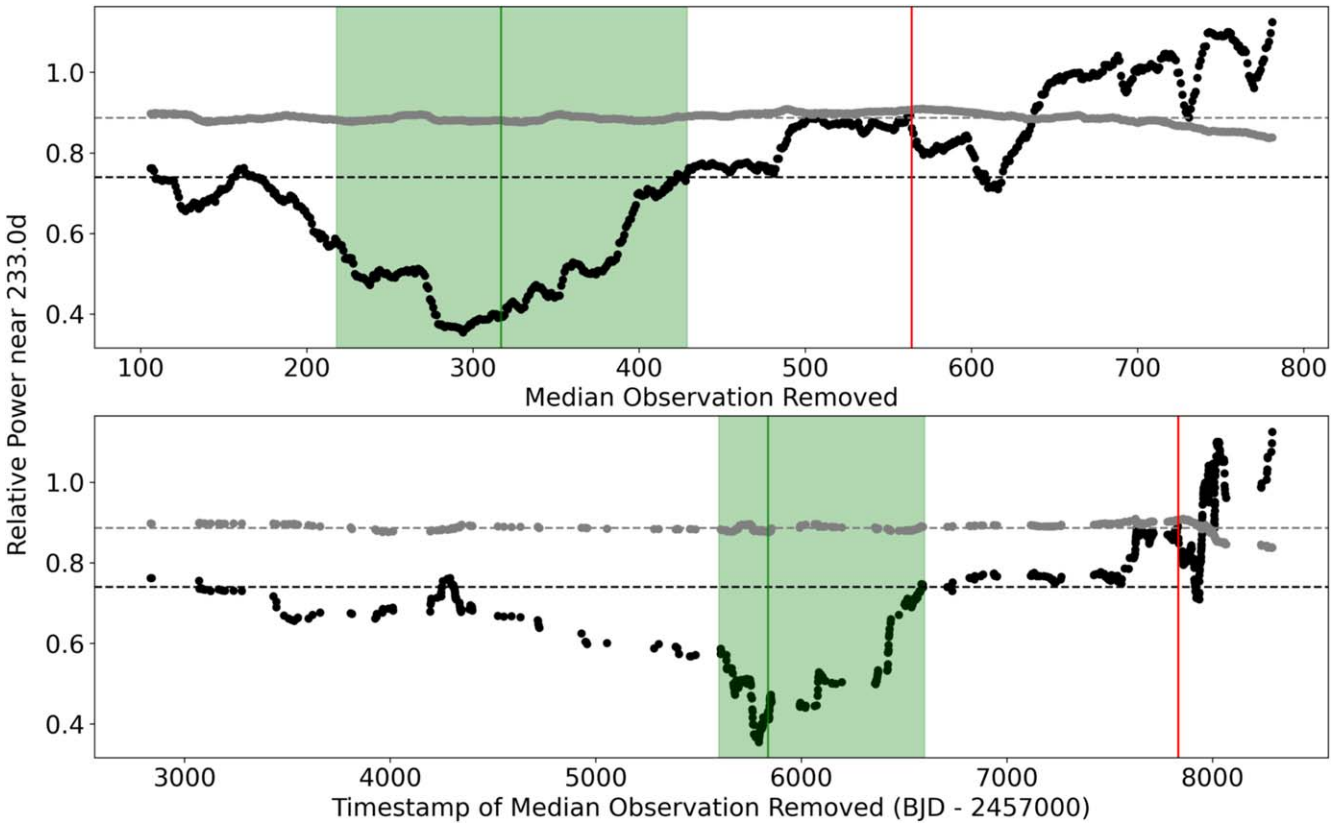

Figure 6. Above: the results from the rolling omission tests in observation number space. Black points are the true updated data set, gray points are an average of 10 synthetic data sets. The green line is the simulation that matches the removal of the 1000 day window points exactly, with green shading to indicate the duration of the 1000 day window. The red line indicates the simulation where the first observation of the 211 consecutive removed observations corresponds to the first CARMENES observation. Below: The same results but in time space.

also that if the signal were persistent in time, our analysis suggests that the most recent observations from CARMENES, HARPS, HARPS-N, and HPF should add power to the 233 day signal if it is caused by an exoplanet when in reality they do not.

4. Discussion

This result is both novel and concerning. It is novel in the sense that there are no examples in the literature of a false-positive exoplanet detection created by a stellar rotation alias longer than the rotation period. Boisse et al. (2010) showed that confidently disentangling planetary signals from stellar-activity-induced signals requires a few circumstances, primarily that the period of the planet signal not be near the stellar rotation period or one of its harmonics. Harmonics, by definition being integer multiples of the frequency, are shorter periods. While false-positive exoplanet signals have also been identified at rotation period aliases, they too tend to fall toward shorter periods (Robertson & Mahadevan 2014), and the same is true for planets where the period is uncertain between two aliases (Dawson & Fabrycky 2010; Robertson 2018). This result has farther-reaching implications for the field of RV exoplanet discovery than just this one system.

Equally, this result is concerning. The exoplanet science community will now have to be as vigilant in scrutinizing the longer aliases of the stellar rotation as it has been for shorter aliases and harmonics. Similarly concerning, this result seems to contradict Extended Data Figure 2 in R18 where they show a stacked periodogram in the fashion of Mortier & Collier Cameron (2017). The figure shows a monotonically rising confidence in the 233 day signal with increased observation. How can we reconcile this figure with our own Figure 6 where we see the signal is localized to a relatively small time and observation space window? An alias is, in itself, a signal that can increase in significance monotonically in the same manner as a planetary signal. Additionally, the periodogram of the first X observations should achieve similar results to the periodogram of the first $X+1$ observations. A better approach would be to stack periodograms of disjoint time spans of the data, similar to our rolling omission test. Along those lines, our rolling omission test is better suited for tracing the localization of a signal in time, which, when used in concert with a stacked periodogram, can provide a more holistic understanding of the nature and veracity of a signal.

We have described the false-positive 233 day exoplanet signal as an "alias" of the 142 day rotation period due to its apparent connection to the stellar rotation and the location of the periodicity near the 1 yr alias of said rotation: $\left(\frac{1}{145}-\frac{1}{365}\right)^{-1}=240$. However, this signal cannot be explained as simply the result of a pure 142 day sinusoid sampled at the irregular cadence and precision of the RV time series. Instead, we believe several factors explain why the rotation signal manifested as observed in RV, Hα, and S_{HK}:

1. During the 1000 day window, the sampling between Hα and S_{HK} observations was not identical but also not too different. Yet the resulting periodograms are very different. In the 1000 day window, the Hα values track

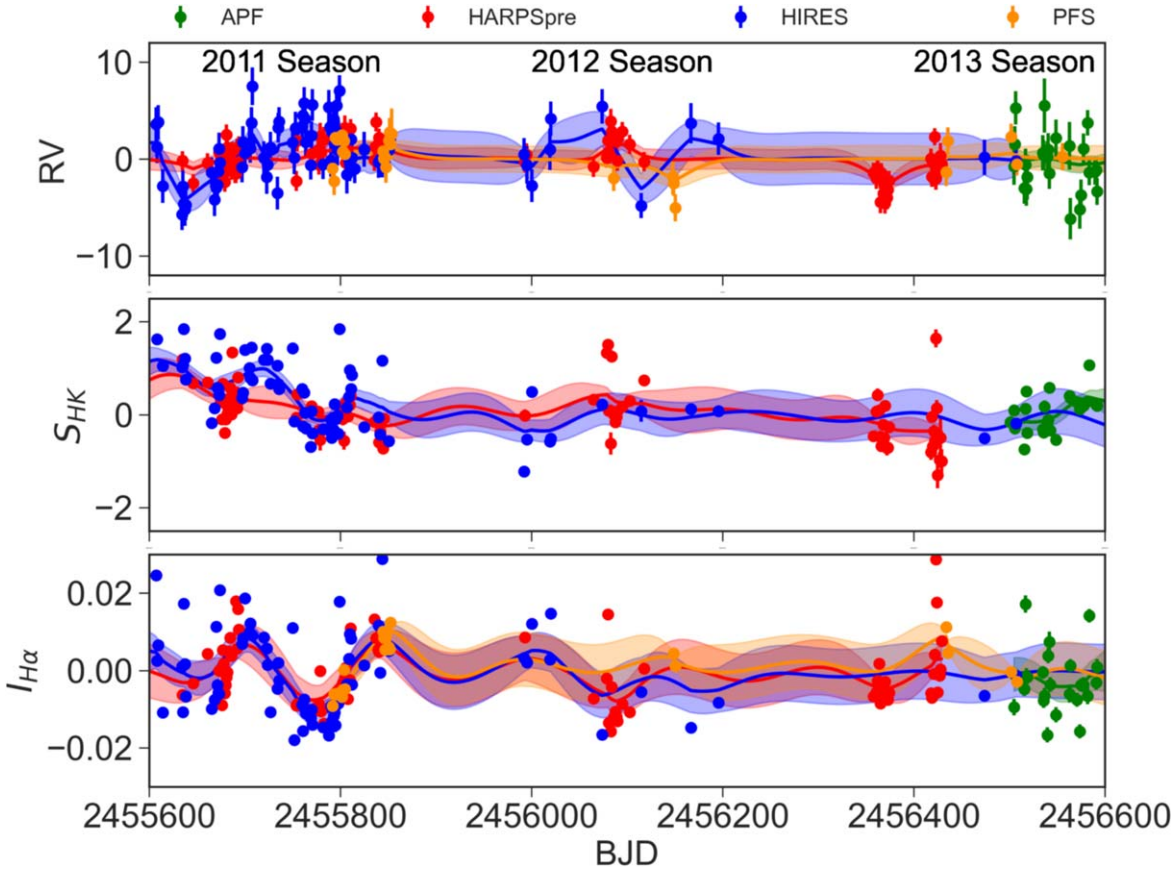

Figure 7. The time series of RV, S_{HK}, and $I_{H\alpha}$ in the 1000 day window with GP functions overlaid with 1σ uncertainty regions. In the first of these observing seasons, 2011, the rotation period of the star is recoverable by eye in S_{HK} and Hα.

a decaying and coherent-across-instruments stellar rotation signal, while the S_{HK} values generally do not; see Figure 7. The S_{HK} shows the rotation period only in the first season, 2011, and in one instrument, HIRES. This might be explained by the low S/N in the continuum of this very red star near the Ca II H&K doublet (Robertson et al. 2016).

2. Hα and S_{HK} often trace different astrophysical phenomena (Gomes da Silva et al. 2014). The activity and periodicity associated with one or the other—or even both—can imprint through to the RVs.
3. The decaying aspect of this signal would make aliasing worse. As shown in Figure 7, the rotation signal during the critical 1000 day window is prominent in the first season, and then slowly decays. Irregular sampling of this decaying, nonsinusoidal signal, alongside any unknown true low-amplitude planet(s), might have created the perfect storm resulting in the false-positive detection of Barnard's star b.

It is crucial that we have a strong understanding of Barnard's star if we are to continue using it as a standard star for commissioning and monitoring red-optical and NIR RV instruments. The star is often considered to be the RV standard for the mid-to-late M-dwarf class. As our spectrometers become capable of breaking through ever-smaller instrumental noise floors, we will need a thorough understanding of the astrophysical variability of any standard star. Barnard's star has always been considered a quiet star, and this is still largely true for signals on the order of a few meters per second and up. But we now see that the stellar activity of Barnard's star will play a role at amplitudes near and below 1 m s^{-1}. If we do not properly understand this stellar activity, then we may not be able to use the star as a standard for commissioning new, ever more sensitive instruments in the future.

As astronomy enters this new era of highly precise instruments capable of detecting exoplanets with RV amplitudes < 1 m s^{-1}, we are excited by the outlook of finding more low-amplitude planets, be they low mass or long period or both. However, long-period planets with small amplitudes in particular will need extra care when the proposed period is close to not only the rotation period of the star or its harmonics but also its longer seasonal aliases. This will be even more important when the period of a proposed signal is nearly as long as the duration of an observing season.

Planetary companions to Barnard's star would be very interesting, not only for their relative proximity to our Sun and therefore enhanced follow-up opportunities but also because the star belongs to an old stellar population. Gizis (1997) classified the star as an "Intermediate Population II" star, which places it somewhere between the halo and the thin disk population of the Milky Way. That said, it would be strange if Barnard's star did not host a planet. We know from planet occurrence rate studies like Dressing & Charbonneau (2015) and Hsu et al. (2020) that planets are common at short periods in M-dwarf systems, though clustering of planets in multi-systems is also seen in both FGK stars (He et al. 2021) and M dwarfs (Ballard & Johnson 2016). Therefore, we might expect Barnard's star to host a planetary system, although, despite ~850 RVs, we may still not be sensitive enough to detect

planets. It is also possible that Barnard's star hosts a nearly face-on planetary system, which would effectively hide any planets from transit or RV searches. Direct imaging with the next generation of large telescopes might help resolve this. R18 states that the separation between the proposed planet and the star would be great enough for Hubble to detect an astrometric signal, which Tal-Or et al. (2019b) confirms and goes on to include Gaia DR2 as an instrument capable of making this measurement. If such measurements are undertaken, based on the result we have presented in this paper, we would not expect a significant signal corresponding to the planet candidate proposed by R18.

With all this in mind, we put effort into searching for a planetary signal in the updated data. We investigated a signal at 45 days, which is seen when removing the 1000 day window observations. However, this signal is concernedly close to the second harmonic of the rotation period; it disappears in the residuals of the GP-only model, and when treated as a planet it is not favored by the model comparison tests (either with or without a GP).

5. Conclusion

The addition of new data from HPF, as well as a suite of tests on the discovery data set, have shown that the 233 day signal is not planetary in origin, rather a transitory one-year alias of the stellar rotation period that took place over a 1000 day time span from 2011 to 2013.

In summary:

1. The 233 day period of the planet candidate proposed by R18 is a one-year alias of the rotation period, $\left(\frac{1}{145}+\frac{1}{365}\right)^{-1}=240$ days. The claimed period of 233 days is well within the 1σ error bars of the rotation period found by Toledo-Padrón et al. (2019) and consistent with our own analysis of the Hα time series.
2. We created various models of the system, taking into account stellar activity and/or a planet. For the updated data set, we have strong evidence ($\Delta\mathrm{BIC}=\sim160$) to reject the planet-only model in favor of an activity-only model. Then, while we can never rule out one or more planets in the system, our analysis finds that the updated data favor the activity-only model over the activity +planet model ($\Delta\mathrm{BIC}=\sim1$).
3. The RV signal at 233 days does not persist through all the tested time windows. Rather, it appears strongly in the middle window, dubbed the 1000 day window from JD 2,455,600 to 2,456,600, comprising 211 observations, while statistically insignificant in the other two windows.
4. The coincidence of the 233 day peak in the RVs and S_{HK} values in the 1000 day window, while absent, otherwise suggests a common stellar activity origin for both signals, aliases of the 145 ± 15 day stellar rotation period.
5. Hα and S_{HK} clearly trace out the stellar rotation period at the beginning of the 1000 day window during the 2011 observing season. The Hα time series in all windows consistently shows a signal at the stellar rotation period.
6. Removing observations from a data set will typically weaken any signal, regardless of its astrophysical origin. We created subsets of the data by randomly removing 211 observations and find that in nearly all simulations the loss of power resulting from this removal is much less than when we remove the specific 211 observations that make up the 1000 day window.
7. Similarly, we removed 211 consecutive RV observations from the full data set, by a process we call Rolling Omission, and found that, again, it is the particular 211 RV observations in the 1000 day window that have the most impact on the strength of the signal. Removing later chunks of data actually increased the power of the signal.

The addition of new data can, and should, change our understanding of any system. Barnard's star is listed in the Guaranteed Time Observations (GTO) lists for the ESPRESSO (Pepe et al. 2010) and NEID (Schwab et al. 2016) exoplanet surveys. The HPF team will also continue to monitor this star. Barnard's star has long fascinated and continually surprised astronomers; we expect this to continue.

We thank the anonymous referee for their thorough and helpful comments on this paper. This work was partially supported by funding from the Center for Exoplanets and Habitable Worlds. The Center for Exoplanets and Habitable Worlds is supported by the Pennsylvania State University, the Eberly College of Science, and the Pennsylvania Space Grant Consortium. This work was supported by NASA Headquarters under the NASA Earth and Space Science Fellowship Program through grant 80NSSC18K1114. We acknowledge support from NSF grants AST-1006676, AST-1126413, AST-1310885, AST-1517592, AST-1310875, AST-1910954, AST-1907622, AST-1909506, ATI 2009889, and ATI 2009982, and the NASA Astrobiology Institute (NNA09DA76A) in our pursuit of precision radial velocities in the NIR. We acknowledge support from the Heising-Simons Foundation via grant 2017-0494. Computations for this research were performed on the Pennsylvania State University's Institute for Computational and Data Sciences' Roar supercomputer. E.B.F. acknowledges the support of the Ambrose Monell Foundation and the Institute for Advanced Study. This work was supported by a grant from the Simons Foundation/SFARI (675601, E.B.F.). The Center for Exoplanets and Habitable Worlds is supported by the Pennsylvania State University and the Eberly College of Science. S.D. acknowledges National Science Foundation AST-1310875 and National Institute of Standards and Technology NIST-on-a-Chip.

These results are based in part on observations obtained with the Habitable-zone Planet Finder Spectrograph on the Hobby–Eberly Telescope. We thank the resident astronomers and telescope operators at the HET for the skillful execution of our observations with HPF, and the HET staff for their dedication to the facility and for enabling these observations. The Hobby–Eberly Telescope is a joint project of the University of Texas at Austin, the Pennsylvania State University, Ludwig-Maximilians-Universität München, and Georg-August Universität Gottingen. The HET is named in honor of its principal benefactors, William P. Hobby and Robert E. Eberly. The HET collaboration acknowledges the support and resources from the Texas Advanced Computing Center.

Facility: HET (Habitable-zone Planet Finder).

Software: `Astropy` (Astropy Collaboration et al. 2013), `barycorrpy` (Kanodia & Wright 2018) `celerite` (Foreman-Mackey et al. 2017), `corner.py` (Foreman-Mackey 2016), `emcee` (Foreman-Mackey et al. 2013), `GNU Parallel` (Tange 2011) `HxRGproc` (Ninan et al. 2018), `Jupyter` (Kluyver et al. 2016), `matplotlib` (Hunter 2007), `numpy`

(Van Der Walt et al. 2011), `pandas` (McKinney 2010), `PyMC3` (Salvatier et al. 2016), `radvel` (Fulton et al. 2018), `SERVAL` (Zechmeister et al. 2018).

Appendix A
HPF RV Extractions

We extract precise RVs from the HPF 1D spectra using the `SERVAL`template-matching RV-extraction code (Zechmeister & Kürster 2009), which we have tailored to work for HPF data as discussed in Metcalf et al. (2019) and Stefansson et al. (2020). To test the robustness of our extracted HPF RVs and accompanying estimated RV uncertainties at these high-precision levels, we performed an additional RV-extraction test. For this test, we performed an RV extraction where we split each HPF spectral order into four separate segments along the four different readout channels on the HPF H2RG detector. We then compared the standard deviation of the RVs derived from the four different segments to the expected standard deviation from our estimated RV uncertainties. In doing so, we noticed that for some observations the standard deviation across the four different segments was slightly higher than expected from our RV uncertainty estimates derived from the inherent RV information content in the HPF spectra and RV template. We suspect this increased level of scatter is due to additional sources of systematic noise in the HPF H2RG detector. H2RGs are known to have a number of systematic noise sources that affect precision RV extractions including bias-level fluctuations, persistence effects, and cross-hatch patterns (see, e.g., Ninan et al. 2018 for a discussion of some of these effects in the HPF H2RG). To account for the additional source of systematic noise we see between the different HPF readout channels, we took the following steps to conservatively increase the estimated RV error bar from the normal SERVAL pipeline.

1. First, as the SERVAL pipeline has been demonstrated to be accurate at the 1 m s^{-1} level in Zechmeister et al. (2018), we extract the HPF RVs order by order using the full RV order. This results in an RV value and RV uncertainty estimate per HPF order. We follow Zechmeister et al. (2017) and Metcalf et al. (2019) and perform a weighted average per RV order.
2. Second, we independently reduce the same spectra by splitting each spectrum into disjoint segments along the four HPF readout channels (512 pixel wide). This yields four independent RV estimates and accompanying RV uncertainties for a given observation after performing a weighted average across all of the orders analyzed (independently for each segment of the spectrum).
3. Third, we modeled the four readout channel RVs (v_i) as statistically independent draws from a Gaussian distribution with the mean equal to the full-order RV (v_f). The Gaussian model's width was set to what we would expect from the reduced information in the readout channel level spectra if the expected error in the full-order RV (σ_f) is multiplied by an unknown inflation factor k, i.e,

$$v_i \sim N(v_f, \sigma_i) \quad \text{where,} \quad \sigma_i = C_i \times (k\sigma_f). \tag{A1}$$

   The reduction in the information content (C_i) due to reducing the size of the spectra into four chunks is $\sim$2. This Bayesian model was implemented in the `pymc3` package (Salvatier et al. 2016) and fitted to each epoch of data. For most of the observations, the inflation factor k was found to be consistent with 1 (implying the scatter in RVs across the four readout channels is consistent with the full-order RV and its derived RV uncertainty). For those epochs where the inflation factor k is greater than 1 with a probability of 95%, we inflated the full-order RV uncertainty by the median of the posterior distribution of the inflation factor k.
4. Lastly, using the newly derived RVs for all of the epochs, we perform a final weighted average of RVs within a given HET track to give a binned RV point and accompanying RV uncertainty per HPF visit.

Using this methodology, of the 1016 unbinned observations, we found that 89 observations have sufficient evidence to increase the RV uncertainty by the inflation factor. Figure 8 compares the RVs and the RV uncertainty of the binned HPF RVs before and after applying this correction to the RV uncertainties. In this binned-by-track view, although a few of the observations have their RV uncertainty increased, the median RV uncertainty remains similar before and after applying this correction. As an additional test, we also tried running all of the same analysis presented in this work with the uninflated RV uncertainties and achieve the same results.

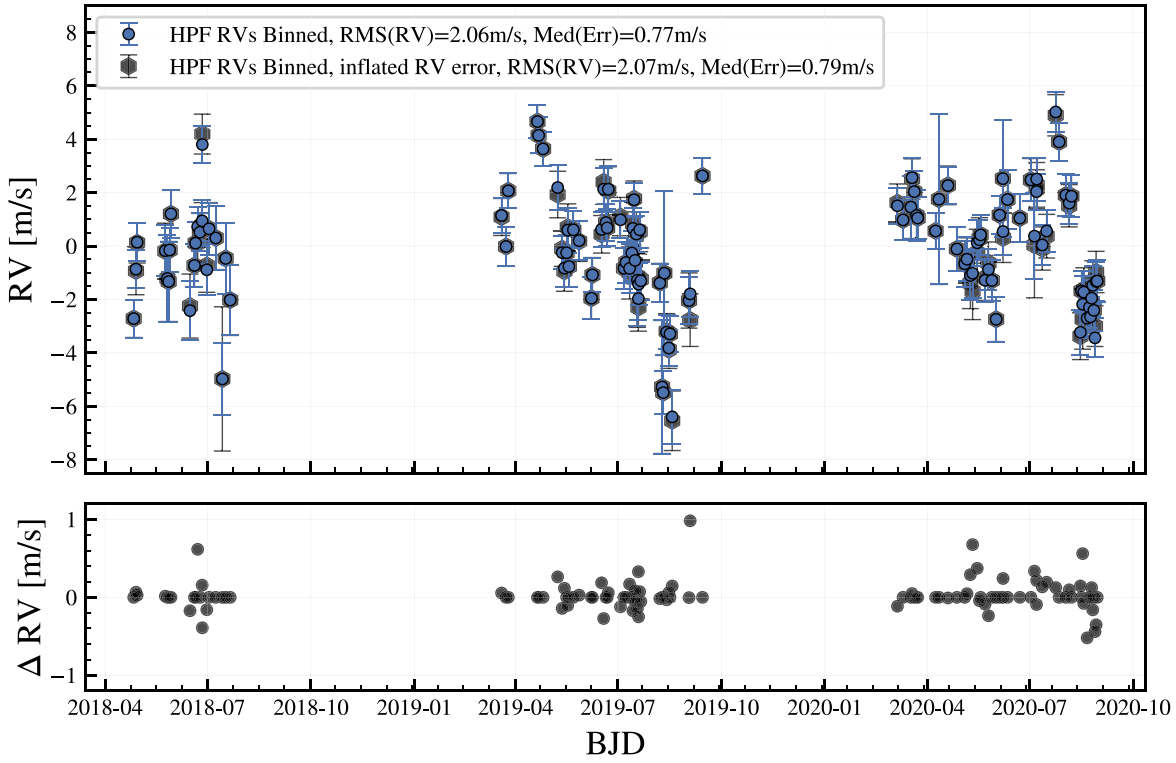

Figure 8. HPF RVs of Barnard's Star before and after accounting for additional RV noise between the different HPF readout channels. We use the inflated RV uncertainties for the final RV analysis.

Appendix B
HPF RVs

Table 1
HPF RV Measurements of Barnard's Star

BJD	RV (m s^{-1})	Err (m s^{-1})	Split
2458234.87812	−3.715	0.709	Pre
2458236.87809	−1.93	0.893	Pre
2458237.87424	−0.881	0.755	Pre
2458561.98905	0.09	0.693	Post
2458565.96692	−1.016	0.743	Post
2458567.96441	1.071	0.648	Post

(This table is available in its entirety in machine-readable form.)

Appendix C
Additional Tables

Table 2
Discovery Data Model Comparison

	Parameters		ΔBIC		
Model	Free Parameters	BIC	GP only	GP + Planet	Planet only
GP only	**26**	**3485.0785**	⋯	−2.040	99.814
GP + Planet	31	3487.1186		⋯	97.774
Planet only	21	3584.8938			⋯

Note. Our preferred model, taking into account ΔBIC, is in bold.

Table 3
Updated Data Model Comparison

	Parameters		ΔBIC		
Model	Free Parameters	BIC	GP + Planet	GP only	Planet only
GP + Planet	40	4021.3900	⋯	1.354	160.970
GP only	**35**	**4022.7433**		⋯	159.616
Planet only	27	4182.3590			⋯

Note. Our preferred model, taking into account ΔBIC, is in bold.

Table 4
Priors and Posteriors for Discovery Hα Data Sets

Model	Parameter	Prior	Posterior
GP	$\log L$	$\mathcal{U}(0.1, 6)$	$1.91^{+0.19}_{-0.19}$
	$\log C$	$\mathcal{U}(-6, 6)$	$-5.44^{+2.60}_{-0.51}$
	$P_{\rm rot}$	$\mathcal{G}(145, 15)$	$142.96^{+11.65}_{-10.49}$
	$\log B$	$\mathcal{U}(-9, 6)$	$-4.28^{+0.08}_{0.08}$
Instrument	$\sigma_{\rm APF}$	$\mathcal{U}(0.001, 1)$	0.01 ± 0.001
	$\sigma_{\rm CARMENES}$	$\mathcal{U}(0.001, 1)$	0.01 ± 0.001
	$\sigma_{\rm HARPSN}$	$\mathcal{U}(0.001, 1)$	0.01 ± 0.001
	$\sigma_{\rm HARPSpre}$	$\mathcal{U}(0.001, 1)$	0.01 ± 0.001
	$\sigma_{\rm HARPSpost}$	$\mathcal{U}(0.001, 1)$	0.01 ± 0.001
	$\sigma_{\rm HIRES}$	$\mathcal{U}(0.001, 1)$	0.01 ± 0.001
	$\sigma_{\rm PFS}$	$\mathcal{U}(0.001, 1)$	0.01 ± 0.001
	$\sigma_{\rm UVES}$	$\mathcal{U}(0.001, 1)$	0.01 ± 0.001
	$\gamma_{\rm APF}$	$\mathcal{U}(-5, 5)$	-0.51 ± 0.001
	$\gamma_{\rm CARMENES}$	$\mathcal{U}(-5, 5)$	-0.52 ± 0.001
	$\gamma_{\rm HARPSN}$	$\mathcal{U}(-5, 5)$	-0.52 ± 0.001
	$\gamma_{\rm HARPSpre}$	$\mathcal{U}(-5, 5)$	-0.51 ± 0.001
	$\gamma_{\rm HARPSpost}$	$\mathcal{U}(-5, 5)$	-0.52 ± 0.001
	$\gamma_{\rm HIRES}$	$\mathcal{U}(-5, 5)$	-0.51 ± 0.001
	$\gamma_{\rm PFS}$	$\mathcal{U}(-5, 5)$	-0.52 ± 0.001
	$\gamma_{\rm UVES}$	$\mathcal{U}(-5, 5)$	-0.51 ± 0.001

Table 5
Priors and Posteriors for Discovery RV Data Sets

Model	Parameter	Prior	GP Only	Planet Only	GP + Planet
GP	$\log L$	$\mathcal{G}(1.91, 0.19)$	$1.60^{+0.15}_{-0.12}$	⋯	$1.56^{+0.18}_{-0.13}$
	$\log C$	$\mathcal{U}(-6, 6)$	$-5.85^{+0.57}_{-0.13}$	⋯	$-5.88^{+0.33}_{-0.10}$
	$P_{\rm rot}$	$\mathcal{G}(142.96, 11.65)$	$141.18^{+12.95}_{-12.45}$	⋯	$139.75^{+14.08}_{-13.79}$
	$\log B_{\rm CARMENES}$	$\mathcal{U}(-2, 2)$	$0.56^{+0.16}_{-0.14}$	⋯	$0.49^{+0.17}_{-0.15}$
	$\log B_{\rm HARPSN}$	$\mathcal{U}(-2, 2)$	$0.51^{+0.25}_{-0.20}$	⋯	$0.56^{+0.23}_{-0.17}$

Table 5
(Continued)

Model	Parameter	Prior	GP Only	Planet Only	GP + Planet
	$\log B_{\rm HARPSpre}$	$\mathcal{U}(-2, 2)$	$0.05^{0.14}_{-0.13}$	⋯	$0.36^{+0.21}_{0.19-}$
	$\log B_{\rm HARPSpost}$	$\mathcal{U}(-2, 2)$	$0.21^{+0.30}_{-0.22}$	⋯	$0.27^{+0.28}_{-0.23}$
	$\log B_{\rm HIRES}$	$\mathcal{U}(-2, 2)$	$0.85^{+0.12}_{-0.12}$	⋯	$0.74^{+0.15}_{-0.14}$
	$\log B_{\rm PFS}$	$\mathcal{U}(-2, 2)$	$0.26^{+0.21}_{-0.34}$	⋯	$-0.01^{+0.23}_{-0.58}$
	$\log B_{\rm UVES}$	$\mathcal{U}(-2, 2)$	$0.70^{+0.11}_{-0.13}$	⋯	$0.67^{+0.12}_{-0.13}$
Instrument	$\sigma_{\rm APF}$	$\mathcal{U}(0.5, 10)$	$2.95^{+0.55}_{-0.45}$	$2.86^{+0.52}_{-0.44}$	$2.88^{0.60}_{-0.48}$
	$\sigma_{\rm CARMENES}$	$\mathcal{U}(0.5, 10)$	$1.16^{+0.19}_{-0.20}$	$1.88^{+0.16}_{-0.14}$	$1.17^{+0.20}_{-0.21}$
	$\sigma_{\rm HARPSN}$	$\mathcal{U}(0.5, 10)$	$0.90^{+0.29}_{-0.23}$	$2.08^{+0.33}_{-0.28}$	$0.90^{+0.29}_{-0.24}$
	$\sigma_{\rm HARPSpre}$	$\mathcal{U}(0.5, 10)$	$0.63^{+0.14}_{-0.09}$	$0.95^{+0.15}_{-0.14}$	$0.66^{+0.16}_{-0.11}$
	$\sigma_{\rm HARPSpost}$	$\mathcal{U}(0.5, 10)$	$0.77^{+0.21}_{-0.17}$	$1.18^{+0.20}_{-0.19}$	$0.75^{+0.23}_{-0.17}$
	$\sigma_{\rm HIRES}$	$\mathcal{U}(0.5, 10)$	$1.32^{+0.30}_{-0.32}$	$2.56^{+0.20}_{-0.19}$	$1.38^{+0.31}_{-0.34}$
	$\sigma_{\rm PFS}$	$\mathcal{U}(0.5, 10)$	$0.79^{+0.39}_{-0.22}$	$1.17^{+0.34}_{-0.32}$	$0.83^{+0.41}_{-0.25}$
	$\sigma_{\rm UVES}$	$\mathcal{U}(0.5, 10)$	$0.75^{+0.28}_{-0.18}$	$2.33^{+0.25}_{-0.22}$	$0.75^{+0.29}_{-0.19}$
	$\gamma_{\rm APF}$	$\mathcal{U}(-10, 10)$	$0.47^{+0.51}_{-0.52}$	$0.21^{+0.48}_{-0.47}$	$0.19^{+0.45}_{-0.47}$
	$\gamma_{\rm CARMENES}$	$\mathcal{U}(-10, 10)$	$2.40^{+0.58}_{-0.62}$	$2.99^{+0.17}_{-0.17}$	$2.36^{+0.54}_{-0.56}$
	$\gamma_{\rm HARPSN}$	$\mathcal{U}(-10, 10)$	$1.67^{+0.80}_{-0.85}$	$2.37^{+0.37}_{-0.37}$	$1.88^{+0.86}_{-0.87}$
	$\gamma_{\rm HARPSpre}$	$\mathcal{U}(-10, 10)$	$-0.75^{+0.28}_{-0.29}$	$-0.43^{+0.13}_{-0.13}$	$-0.61^{+0.21}_{-0.23}$
	$\gamma_{\rm HARPSpost}$	$\mathcal{U}(-10, 10)$	$2.97^{+0.82}_{-0.83}$	$3.44^{+0.23}_{-0.23}$	$3.30^{+0.88}_{-0.95}$
	$\gamma_{\rm HIRES}$	$\mathcal{U}(-10, 10)$	$0.89^{+0.46}_{-0.49}$	$-0.65^{+0.23}_{-0.23}$	$-0.89^{+0.44}_{-0.44}$
	$\gamma_{\rm PFS}$	$\mathcal{U}(-10, 10)$	$0.38^{+0.42}_{-0.42}$	$0.36^{+0.29}_{-0.29}$	$0.25^{+0.34}_{-0.33}$
	$\gamma_{\rm UVES}$	$\mathcal{U}(-10, 10)$	$1.46^{+0.49}_{-0.50}$	$1.75^{+0.30}_{-0.30}$	$1.45^{+0.49}_{-0.48}$
Planet	Period	$\mathcal{G}(233, 15)$	⋯	$232.86^{+0.29}_{-0.43}$	$232.64^{+0.32}_{-0.39}$
	T_c	$\mathcal{G}(2454937.92, 20)$	⋯	$2454934.03^{+4.55}_{-4.01}$	$2454936.11^{+4.24}_{-4.33}$
	$K_{\rm amp}$	$\mathcal{U}(0.3, 10)$	⋯	$1.16^{+0.12}_{-0.12}$	$1.16^{+0.22}_{-0.23}$
	$\sqrt{e}\ sin\omega$	$\mathcal{U}(-1, 1)$	⋯	$0.53^{+0.09}_{-0.13}$	$0.59^{+0.12}_{-0.22}$
	$\sqrt{e}\ cos\omega$	$\mathcal{U}(-1, 1)$	⋯	$-0.16^{+0.19}_{-0.18}$	$-0.08^{+0.21}_{-0.20}$

Table 6
Priors and Posteriors for Updated RV Data Sets

Model	Parameter	Prior	GP Only	Planet Only	GP + Planet
GP	$\log L$	$\mathcal{G}(1.91, 0.19)$	$1.56^{+0.13}_{-0.09}$	⋯	$1.52^{+0.14}_{-0.09}$
	$\log C$	$\mathcal{U}(-6, 6)$	$-5.92^{+0.18}_{-0.06}$	⋯	$-5.92^{+0.16}_{-0.06}$
	$P_{\rm rot}$	$\mathcal{G}(142.96, 11.65)$	$142.78^{+13.41}_{-13.93}$	⋯	$139.36^{+14.56}_{-14.76}$
	$\log B_{\rm CARMENES}$	$\mathcal{U}(-2, 2)$	$0.54^{+0.15}_{-0.12}$	⋯	$0.48^{+0.16}_{-0.12}$
	$\log B_{\rm HARPSN}$	$\mathcal{U}(-2, 2)$	$0.48^{+0.22}_{-0.17}$	⋯	$0.57^{+0.19}_{-0.14}$
	$\log B_{\rm HARPSpre}$	$\mathcal{U}(-2, 2)$	$0.25^{+0.13}_{-0.11}$	⋯	$-0.11^{+0.18}_{-0.13}$
	$\log B_{\rm HARPSpost}$	$\mathcal{U}(-2, 2)$	$0.52^{+0.26}_{-0.16}$	⋯	$0.62^{+0.22}_{-0.17}$
	$\log B_{\rm HIRESpre}$	$\mathcal{U}(-2, 2)$	$0.94^{+0.19}_{-0.17}$	⋯	$0.85^{+0.19}_{-0.17}$
	$\log B_{\rm HIRESpost}$	$\mathcal{U}(-2, 2)$	$0.81^{+0.14}_{-0.14}$	⋯	$0.59^{+0.18}_{-0.15}$
	$\log B_{\rm PFS}$	$\mathcal{U}(-2, 2)$	$0.28^{+0.16}_{-0.27}$	⋯	$-0.01^{+0.19}_{-0.31}$
	$\log B_{\rm UVES}$	$\mathcal{U}(-2, 2)$	$0.71^{+0.11}_{-0.11}$	⋯	$0.67^{+0.10}_{-0.12}$
	$\log B_{\rm HPFpre}$	$\mathcal{U}(-2, 2)$	$-1.91^{+0.19}_{-0.07}$	⋯	$-1.93^{+0.16}_{-0.06}$
	$\log B_{\rm HPFpost}$	$\mathcal{U}(-2, 2)$	$0.64^{+0.13}_{-0.11}$	⋯	$0.64^{+0.14}_{-0.11}$
Instrument	$\sigma_{\rm APF}$	$\mathcal{U}(0.5, 10)$	$2.97^{+0.61}_{-0.50}$	$2.88^{+0.53}_{-0.46}$	$2.89^{+0.61}_{-0.50}$
	$\sigma_{\rm CARMENES}$	$\mathcal{U}(0.5, 10)$	$1.15^{+0.20}_{-0.21}$	$1.86^{+0.16}_{-0.15}$	$1.16^{+0.20}_{-0.21}$
	$\sigma_{\rm HARPSN}$	$\mathcal{U}(0.5, 10)$	$0.91^{+0.29}_{-0.24}$	$2.07^{+0.33}_{-0.28}$	$0.89^{+0.31}_{-0.23}$
	$\sigma_{\rm HARPSpre}$	$\mathcal{U}(0.5, 10)$	$0.93^{+0.16}_{-0.15}$	$1.43^{+0.14}_{-0.13}$	$0.96^{+0.17}_{-0.15}$
	$\sigma_{\rm HARPSpost}$	$\mathcal{U}(0.5, 10)$	$1.04^{+0.23}_{-0.22}$	$1.67^{+0.22}_{-0.19}$	$1.02^{+0.25}_{-0.24}$
	$\sigma_{\rm HIRESpre}$	$\mathcal{U}(0.5, 10)$	$1.58^{+0.55}_{-0.52}$	$2.82^{+0.40}_{-0.35}$	$1.65^{+0.54}_{-0.53}$
	$\sigma_{\rm HIRESpost}$	$\mathcal{U}(0.5, 10)$	$1.51^{+0.32}_{-0.33}$	$2.46^{+0.23}_{-0.21}$	$1.61^{+0.32}_{-0.33}$
	$\sigma_{\rm PFS}$	$\mathcal{U}(0.5, 10)$	$0.77^{+0.36}_{-0.21}$	$1.30^{+0.36}_{-0.33}$	$0.77^{+0.38}_{-0.21}$
	$\sigma_{\rm UVES}$	$\mathcal{U}(0.5, 10)$	$0.74^{+0.29}_{-0.18}$	$2.39^{+0.25}_{-0.22}$	$0.71^{+0.28}_{-0.16}$
	$\sigma_{\rm HPFpre}$	$\mathcal{U}(0.5, 10)$	$1.38^{+0.41}_{-0.31}$	$1.31^{+0.38}_{-0.31}$	$1.27^{+0.43}_{-0.32}$
	$\sigma_{\rm HPFpost}$	$\mathcal{U}(0.5, 10)$	$0.59^{+0.14}_{-0.07}$	$1.87^{+0.19}_{-0.16}$	$0.59^{+0.13}_{-0.07}$

Table 6
(Continued)

Model	Parameter	Prior	GP Only	Planet Only	GP + Planet
	$\gamma_{\rm APF}$	$\mathcal{U}(-10, 10)$	$0.48^{+0.47}_{-0.50}$	$0.23^{+0.46}_{-0.47}$	$0.28^{+0.40}_{-0.42}$
	$\gamma_{\rm CARMENES}$	$\mathcal{U}(-10, 10)$	$2.43^{+0.57}_{-0.59}$	$2.99^{+0.17}_{-0.17}$	$2.37^{+0.56}_{-0.59}$
	$\gamma_{\rm HARPSN}$	$\mathcal{U}(-10, 10)$	$1.68^{+0.75}_{-0.84}$	$2.21^{+0.37}_{-0.38}$	$1.82^{+0.86}_{-0.90}$
	$\gamma_{\rm HARPSpre}$	$\mathcal{U}(-10, 10)$	$-0.67^{+0.32}_{-0.34}$	$-0.25^{+0.16}_{-0.16}$	$-0.50^{+0.25}_{-0.26}$
	$\gamma_{\rm HARPSpost}$	$\mathcal{U}(-10, 10)$	$-0.86^{+0.90}_{-1.01}$	$-0.37^{+0.25}_{-0.27}$	$-0.47^{+0.92}_{-0.79}$
	$\gamma_{\rm HIREspre}$	$\mathcal{U}(-10, 10)$	$-1.40^{+0.79}_{-0.79}$	$-1.55^{+0.44}_{-0.43}$	$-1.45^{+0.70}_{-0.75}$
	$\gamma_{\rm HIRESpost}$	$\mathcal{U}(-10, 10)$	$-0.34^{+0.45}_{-0.47}$	$-0.14^{+0.23}_{-0.23}$	$-0.32^{+0.35}_{-0.40}$
	$\gamma_{\rm PFS}$	$\mathcal{U}(-10, 10)$	$0.34^{+0.38}_{-0.39}$	$-0.37^{+0.30}_{-0.30}$	$0.26^{+0.33}_{-0.31}$
	$\gamma_{\rm UVES}$	$\mathcal{U}(-10, 10)$	$1.46^{+0.50}_{-0.49}$	$1.78^{+0.30}_{-0.30}$	$1.44^{+0.48}_{-0.50}$
	$\gamma_{\rm HPFpre}$	$\mathcal{U}(-10, 10)$	$-1.20^{+0.39}_{-0.42}$	$-0.90^{+0.39}_{-0.40}$	$-0.99^{+0.42}_{-0.43}$
	$\gamma_{\rm HPFpost}$	$\mathcal{U}(-10, 10)$	$0.51^{+0.59}_{-0.59}$	$-1.04^{+0.22}_{-0.22}$	$-0.58^{+0.54}_{-0.62}$
Planet	Period	$\mathcal{G}(233, 15)$	⋯	$231.93^{+0.49}_{-0.30}$	$232.36^{+0.17}_{-0.22}$
	T_c	$\mathcal{G}(2454937.92, 20)$	⋯	$2454920.91^{+6.29}_{-7.01}$	$2454935.87^{+2.30}_{-2.96}$
	$K_{\rm amp}$	$\mathcal{U}(0.3, 10)$	⋯	$1.19^{+0.13}_{-0.13}$	$1.28^{+0.28}_{-0.28}$
	$\sqrt{e}\sin\omega$	$\mathcal{U}(-1, 1)$	⋯	$0.10^{+0.20}_{-0.23}$	$0.60^{+0.12}_{-0.21}$
	$\sqrt{e}\cos\omega$	$\mathcal{U}(-1, 1)$	⋯	$0.28^{+0.16}_{-0.25}$	$-0.24^{+0.21}_{-0.16}$

ORCID iDs

Jack Lubin https://orcid.org/0000-0001-8342-7736
Paul Robertson https://orcid.org/0000-0003-0149-9678
Gudmundur Stefansson https://orcid.org/0000-0001-7409-5688
Joe Ninan https://orcid.org/0000-0001-8720-5612
Suvrath Mahadevan https://orcid.org/0000-0001-9596-7983
Michael Endl https://orcid.org/0000-0002-7714-6310
Eric Ford https://orcid.org/0000-0001-6545-639X
Jason T. Wright https://orcid.org/0000-0001-6160-5888
Corey Beard https://orcid.org/0000-0001-7708-2364
Chad Bender https://orcid.org/0000-0003-4384-7220
William D. Cochran https://orcid.org/0000-0001-9662-3496
Scott A. Diddams https://orcid.org/0000-0002-2144-0764
Connor Fredrick https://orcid.org/0000-0002-0560-1433
Samuel Halverson https://orcid.org/0000-0003-1312-9391
Shubham Kanodia https://orcid.org/0000-0001-8401-4300
Andrew J. Metcalf https://orcid.org/0000-0001-5000-1018
Lawrence Ramsey https://orcid.org/0000-0002-4289-7958
Arpita Roy https://orcid.org/0000-0001-8127-5775
Christian Schwab https://orcid.org/0000-0002-0091-7105
Ryan Terrien https://orcid.org/0000-0002-4788-8858

References

Anglada-Escudé, G., & Butler, R. P. 2012, ApJS, 200, 15
Angus, R., Morton, T., Aigrain, S., Foreman-Mackey, D., & Rajpaul, V. 2018, MNRAS, 474, 2094
Astropy Collaboration, Robitaille, T. P., Tollerud, E. J., et al. 2013, AAP, 558, A33
Bailer-Jones, C. A. L., Rybizki, J., Fouesneau, M., Mantelet, G., & Andrae, R. 2018, AJ, 156, 58
Ballard, S., & Johnson, J. A. 2016, ApJ, 816, 66
Barnard, E. E. 1916, AJ, 29, 181
Bean, J. L., Seifahrt, A., Hartman, H., et al. 2010, ApJ, 713, 410
Benedict, G. F., McArthur, B., Chappell, D. W., et al. 1999, AJ, 118, 1086
Berdiñas, Z. M., Rodríguez-López, C., Amado, P. J., Anglada-Escude, G., et al. 2017, MNRAS, 469, 4268
Boisse, I., Bouchy, F., Hébrard, G., et al. 2010, in IAU Symp. 273, The Physics of Sun and Star Spots (Cambridge: Cambridge Univ. Press), 281
Bortle, A., Fausey, H., Ji, J., et al. 2021, AJ, 161, 230
Butler, R. P., Marcy, G. W., Williams, E., et al. 1996, PASP, 108, 500
Choi, J., McCarthy, C., Marcy, G. W., et al. 2013, ApJ, 764, 131
Cosentino, R., Lovis, C., Pepe, F., et al. 2012, Proc. SPIE, 8446, 657
Crane, J. D., Shectman, S. A., Butler, R. P., et al. 2010, Proc. SPIE, 7735, 1909
Davenport, J. R. A., Mendoza, G. T., & Hawley, S. L. 2020, AJ, 160, 36
Dawson, R. I., & Fabrycky, D. C. 2010, ApJ, 722, 937
Dekker, H., D'Odorico, S., Kaufer, A., Delabre, B., & Kotzlowski, H. 2000, Proc. SPIE, 4008, 534
Dressing, C. D., & Charbonneau, D. 2015, ApJ, 807, 45
Feng, F., Tuomi, M., & Jones, H. R. A. 2017, MNRAS, 470, 4794
Foreman-Mackey, D. 2016, JOSS, 1, 24
Foreman-Mackey, D., Agol, E., Ambikasaran, S., & Angus, R. 2017, AJ, 154, 220
Foreman-Mackey, D., Hogg, D. W., Lang, D., & Goodman, J. 2013, PASP, 125, 306
Fulton, B. J., Petigura, E. A., Blunt, S., & Sinukoff, E. 2018, PASP, 130, 044504
Gaia Collaboration 2018, yCat, I/345
Gaia Collaboration, Smart, R. L., Sarro, L. M., et al. 2021, A&A, 649, A6
Gatewood, G., & Eichhorn, H. 1973, AJ, 78, 769
Giles, H. A. C., Collier Cameron, A., & Haywood, R. D. 2017, MNRAS, 472, 1618
Gizis, J. E. 1997, AJ, 113, 806
Gomes da Silva, J., Santos, N. C., Boisse, I., Dumusque, X., & Lovis, C. 2014, A&A, 566, A66
Hara, N. C., Boué, G., Laskar, J., & Correia, A. C. M. 2017, MNRAS, 464, 1220
Hatzes, A. P. 2013, ApJ, 770, 133
Haywood, R. D., Collier Cameron, A., Queloz, D., et al. 2014, MNRAS, 443, 2517
He, M. Y., Ford, E. B., & Ragozzine, D. 2021, AJ, 161, 16
Hershey, J. L. 1973, AJ, 78, 421
Hsu, D. C., Ford, E. B., & Terrien, R. 2020, MNRAS, 498, 2249
Hunter, J. D. 2007, CSE, 9, 90
Kanodia, S., & Wright, J. 2018, RNAAS, 2, 4
Kaplan, K. F., Bender, C. F., Terrien, R., et al. 2018, in The 28th Int. Astronomical Data Analysis Software and Systems
Kass, R. E., & Raftery, A. E. 1995, J. Am. Stat. Assoc., 90, 773
Kluyver, T., Ragan-Kelley, B., Pérez, F., et al. 2016, in Positioning and Power in Academic Publishing: Players, Agents and Agendas, ed. F. Loizides & B. Scmidt (IOS Press), 87, https://eprints.soton.ac.uk/403913/
Kopparapu, R. K., Ramirez, R., Kasting, J. F., et al. 2013, ApJ, 765, 131
Kürster, M., Endl, M., Rouesnel, F., et al. 2003, A&A, 403, 1077
Lo Curto, G., Pepe, F., Avila, G., et al. 2015, Msngr, 162, 9
Mahadevan, S., Ramsey, L., Bender, C., et al. 2012, Proc. SPIE, 8446, 84461S
Mahadevan, S., Ramsey, L. W., Terrien, R., et al. 2014, Proc. SPIE, 9147, 91471G

Marchwinski, R. C., Mahadevan, S., Robertson, P., Ramsey, L., & Harder, J. 2015, ApJ, 798, 63
Mayor, M., Pepe, F., Queloz, D., et al. 2003, Msngr, 114, 20
McKinney, W. 2010, in Proc. 9th Python in Science Conf., ed. S. van der Walt & J. Millman, 51
McQuillan, A., Mazeh, T., & Aigrain, S. 2014, ApJS, 211, 24
Metcalf, A. J., Anderson, T., Bender, C. F., et al. 2019, Optica, 6, 233
Mortier, A., & Collier Cameron, A. 2017, A&A, 601, A110
Newton, E. R., Irwin, J., Charbonneau, D., et al. 2016a, ApJ, 821, 93
Newton, E. R., Irwin, J., Charbonneau, D., Berta-Thompson, Z. K., & Dittmann, J. A. 2016b, ApJL, 821, L19
Nielsen, M. B., Gizon, L., Schunker, H., & Karoff, C. 2013, A&A, 557, L10
Ninan, J. P., Bender, C. F., Mahadevan, S., et al. 2018, Proc. SPIE, 10709, 107092U
Pepe, F. A., Cristiani, S., Rebolo Lopez, R., et al. 2010, Proc. SPIE, 7735, 77350F
Quirrenbach, A., Amado, P. J., Caballero, J. A., et al. 2016, Proc. SPIE, 9908, 296
Rajpaul, V., Aigrain, S., Osborne, M. A., Reece, S., & Roberts, S. 2015, MNRAS, 452, 2269
Reiners, A., Bean, J. L., Huber, K. F., et al. 2010, ApJ, 710, 432
Ribas, I., Tuomi, M., Reiners, A., et al. 2018, Natur, 563, 365
Robertson, P. 2018, ApJL, 864, L28
Robertson, P., Bender, C., Mahadevan, S., Roy, A., & Ramsey, L. W. 2016, ApJ, 832, 112
Robertson, P., & Mahadevan, S. 2014, ApJL, 793, L24
Robertson, P., Mahadevan, S., Endl, M., & Roy, A. 2014, Sci, 345, 440
Robertson, P., Roy, A., & Mahadevan, S. 2015, ApJL, 805, L22
Robertson, P., Stefansson, G., Mahadevan, S., et al. 2020, ApJ, 897, 125
Salvatier, J., Wiecki, T. V., & Fonnesbeck, C. 2016, PeerJ Comput. Sci., 2, e55
Schwab, C., Rakich, A., Gong, Q., et al. 2016, Proc. SPIE, 9908, 99087H
Shetrone, M., Cornell, M. E., Fowler, J. R., et al. 2007, PASP, 119, 556
Stefansson, G., Cañas, C., Wisniewski, J., et al. 2020, AJ, 159, 100
Stefansson, G., Hearty, F., Robertson, P., et al. 2016, ApJ, 833, 175
Suárez Mascareño, A., Faria, J. P., Figueira, P., et al. 2020, A&A, 639, A77
Suárez Mascareño, A., Rebolo, R., González Hernández, J. I., et al. 2018, A&A, 612, A89
Tal-Or, L., Trifonov, T., Zucker, S., Mazeh, T., & Zechmeister, M. 2019a, MNRAS, 484, L8
Tal-Or, L., Zucker, S., Ribas, I., Anglada-Escudé, G., & Reiners, A. 2019b, A&A, 623, A10
Tange, O. 2011, login: The USENIX Magazine, 36, 42
Toledo-Padrón, B., González Hernández, J. I., Rodríguez-López, C., et al. 2019, MNRAS, 488, 5145
Trifonov, T., Tal-Or, L., Zechmeister, M., et al. 2020, A&A, 636, A74
Valenti, J. A., Butler, R. P., & Marcy, G. W. 1995, PASP, 107, 966
van de Kamp, P. 1963, AJ, 68, 515
van de Kamp, P. 1969, AJ, 74, 757
van de Kamp, P. 1975, AJ, 80, 658
van de Kamp, P. 1982, VA, 26, 141
Van Der Walt, S., Colbert, S. C., & Varoquaux, G. 2011, CSE, 13, 22
Vanderburg, A., Plavchan, P., Johnson, J. A., et al. 2016, MNRAS, 459, 3565
Vogt, S. S., Allen, S. L., Bigelow, B. C., et al. 1994, Proc. SPIE, 2198, 362
Vogt, S. S., Radovan, M., Kibrick, R., et al. 2014, PASP, 126, 359
Wright, J. T., & Eastman, J. D. 2014, PASP, 126, 838
Zechmeister, M., & Kürster, M. 2009, A&A, 496, 577
Zechmeister, M., Kürster, M., & Endl, M. 2009, A&A, 505, 859
Zechmeister, M., Reiners, A., Amado, P. J., et al. 2018, A&A, 609, A12
Zechmeister, M., Reiners, A., Amado, P. J., et al. 2017, A&A, 609, A12